Comparison of melting in three and two dimensions: Microscopy of colloidal spheres

C. A. Murray, W. O. Sprenger, and R. A. Wenk
AT&T Bell Laboratories, Murray Hill, New Jersey 07974
(Received 5 January 1990)

Digital imaging is used to study the instantaneous particle positions and trajectories of highly charged monodisperse 0.3-μm-diam polystyrene spheres in water suspension. We find that a three-dimensional fcc crystal near a smooth glass wall melts abruptly into a layered fluid as a function of the in-plane sphere density parallel to the wall. In contrast, a single two-dimensional layer of the identical colloid confined between two smooth glass walls exhibits a gradual two-stage melting transition in which there are separate divergences of translational and orientational order.

I. INTRODUCTION

A. Predictions of melting in two and three dimensions

Freezing and melting are basic physical phenomena that are yet to be thoroughly understood theoretically. Evidence for the universal geometrical nature of the melting transition comes from computer simulations and experiments. A system of hard spheres was discovered in simulations almost three decades ago[1] to have a first-order crystal-fluid transition that is very similar to the melting transitions of real substances. This brought about a revival of the van der Waals picture of liquids[2] in which it is assumed the dominant influence on the local structural arrangements of molecules in a liquid is their short-range nearly-hard-sphere-like repulsive interactions. The structure factor $S(q)$ of dense fluids is very similar to that of the hard-sphere system near freezing; in particular for many three-dimensional (3D) liquids Verlet's rule[3] holds: the value of $S(q=q_{\max})$ at the first peak is between 2.8 and 3.1 just before freezing. In the 3D crystal before melting, Lindemann's criterion[4] appears to hold nearly universally as well: the crystal melts when the root-mean-square displacements of atoms about their equilibrium positions become larger than about $0.1a$, where a is the interatomic separation.

Theories of melting or freezing can be loosely categorized into three types: (i) those that address the absolute instability of the solid (basically Lindemann's criterion)—for example, a shear instability in self-consistent phonons;[5] (ii) those that introduce the spontaneous generation of lattice defects that eventually cause enough disorder to melt the solid—for example, dislocations,[6] disclinations,[6,7] or grain boundaries;[8] and (iii) those that introduce[9] density waves as order-parameter modes in a fluid to obtain freezing criteria similar to Verlet's rule. It has been pointed out by Kosterlitz, Thouless, Halperin, Nelson, and Young[6] (KTHNY) that a two-dimensional (2D) crystal is considerably more unstable with respect to fluctuations such as topological lattice defects than its 3D analog. Their prediction of two continuous melting transitions for a 2D crystal instead of the single well-known first-order transition in 3D has generated much controversy, experimental search, and computer simulations for the last decade and a half.[10] The two transitions they predict are caused by the separate disappearance of first, the translational, and then later, the orientational order parameters of the system. The separate phase into which the 2D triangular crystal first melts in the KTHNY scenario has been called the "hexatic," as it has short-range translational order accompanied by long-range slow algebraic decay of sixfold orientational order. The hexatic then melts into an ordinary isotropic fluid for which there is an exponential decay of translational and orientational order on the same distance scale. An excellent review of the many consequences of this elegant theory is given by Nelson.[11]

Until recently, little or no consensus existed from experiments or computer simulations[10] for the existence of continuous melting transitions in 2D or the existence of a hexatic phase in systems of spherically symmetric particles—although tilted hexatics, in which the tilt and orientation of long rod molecules in the plane are coupled, have been well established in 3D layered[12] and more recently 2D (Ref. 13) liquid crystals. In this paper we contrast the melting of a model experimental system of highly charged submicron spheres in a colloidal suspension rigidly confined to 2D with the melting of the same system in 3D near a smooth wall. We show that there is a qualitative difference in the nature of the melting transition determined by dimensionality alone in this system—all other experimental parameters remaining constant.

B. Monodisperse colloids as a model system

Monodisperse latex spheres are a fascinating model experimental system. They have been used as a model condensed matter system for more than a decade.[14] They can be obtained with diameter and sphericity dispersions as small as 1%,[15] and comparable corresponding surface charge uniformities. The sphere-sphere interactions are in general complex, as they include van der Waals, hard sphere, screened Coulomb, and many-body hydrodynamic contributions.[16] The experimental 3D phase diagram of the colloids[17] is qualitatively similar to that found[18] for a molecular dynamics simulation of hard spheres in-

teracting with Yukawa potentials with an effective sphere charge much smaller than the actual titratable charge. For our purposes here, at the sphere densities and charges relevant to this experiment, the repulsive screened Coulomb and indirect hydrodynamic interactions are the most important. The sphere-glass wall interaction is also very important. It is predominantly repulsive at the sphere-wall separations of the experiment because of the positive image charges of the spheres as well as dissociated OH groups on the glass surface, charged with the same sign as the surface sulfate groups on our spheres.

A few years ago[19] we began studying in detail the melting transition of a 2D layer of uniform submicron spheres in colloidal suspension by the use of digital imaging. Instead of simply relying on snapshots of the colloid structure[20] or diffraction from the 2D system,[21] we set out to make use of the power of direct imaging of individual particle motions and also topological lattice defects in both space and time. Since that time there have been a number of other similar imaging studies of melting of single layers of slightly larger colloidal spheres.[22,23] We chose to study melting of submicron spheres for several reasons. As in simulations, it is possible to create a substrate that is perfectly smooth on the colloidal scale, unlike the case in atomic experiments where the modulation of a graphite substrate, for example, is unavoidable and can have very large effects on the orientational order and phase diagram of a rare gas overlayer.[24] We note that a smooth, hard substrate is also the limit of most theoretical models of wetting as well.[25] It is also possible to confine the spheres rigidly into a plane between two parallel plates so that out-of-plane motions and second-layer promotion are entirely avoided near melting. These could have a drastic effect on the melting transition.[26]

In a colloid experiment, one can also alleviate many of the problems with computer simulations associated with insufficient equilibration times or periodic boundary conditions by studying a small portion of a much larger system, and allowing the entire system of fluid, crystal, and reservoir to come to statistical equilibration in direct contact. If the latex spheres are comparable in size to ~ 1 μm, they exhibit Brownian motion and thus have a true thermodynamic temperature[27] unlike larger particles used for analog simulations such as ball bearings. Also, the relevant time and length scales for both individual particle motion and equilibration are reasonably accessible in the laboratory with optical-video microscopy for colloidal particles of this size in water suspension. In these digital imaging experiments we essentially use the colloid as an "analog" molecular dynamics computer in which the particles obey Brownian dynamics with repulsive interactions.

A summary of our earlier experiments on the melting of 2D colloidal layers is given in Murray and Wenk.[28] In these 2D experiments we used colloidal spheres of diameter $d=0.305$ μm and surface charge $\sim 2\times 10^4$ electrons per sphere with a size uniformity of $\sim 2\%$. the bulk fcc-bcc phase transition takes place in that fully ionized colloid at a nearest-neighbor separation distance of $a=(2.97\pm 0.1)d$ in the fcc crystal. The 2D layer melting was studied in contact with a bulk reservoir somewhat denser than the fcc-bcc transition density for fully deionized spheres. The 2D melting transition was observed at $a=(2.5\pm 0.05)d$. Using the fcc-bcc phase boundary at the limit of no added salt to map onto the Yukawa phase diagram of Robbins *et al.*,[18] we obtain an estimate of the effective charge and effective screening length of these spheres as $Z^*\sim 750$ electrons and $\lambda\sim 0.29$ μm, respectively, at the fcc-bcc transition in the bulk. This, of course, only give a very rough estimate of the screened Coulomb interaction between spheres as the mapping onto the Yukawa phase diagram is a gross oversimplification. However, it is helpful to make a comparison between this lower charged colloid and the colloid used in the present 2D and 3D melting experiments.

In the new experiments described here, we use colloidal spheres of the same diameter and size uniformity as in the earlier experiments, but with a titratable charge roughly five times higher. The bulk fcc-bcc phase transition is observed at a fcc nearest-neighbor separation of $a=(4.4\pm 0.09)d$ with no added salt, which is close to the density of the 3D reservoir in contact with our 2D sample. The 2D melting transition takes place in the new experiments at $a=(4.3\pm 0.05)d$—an in-plane density roughly a third that of the earlier experiments. Again, mapping as before on the Yukawa phase diagram in the limit of no added salt for the 3D fcc-bcc transition, we obtain a rough estimate for the effective charge per sphere and screening length of $Z^*\sim 1000$ electrons and $\lambda\sim 0.35$ μm, respectively, at this density. For the 2D experiments, the newer colloid has a somewhat longer-ranger interaction than the old. We estimate the screening parameter Λ to be roughly 2.93 for the new colloid and roughly 3.49 for the old colloid in the 2D crystal just before melting. Here $\Lambda=a_s/\lambda$, with $a_s^3=n_{3D}$, computed for a unit cell of the system of the 2D layer and image charge layers.

The paper is organized as follows: In Sec. II we summarize the experimental and data analysis procedures that are common to the 3D and 2D melting experiments. In Sec. III, we describe the 3D experimental geometry and then present the results of the melting of a 3D fcc crystal near a smooth glass surface as a function of in-plane sphere density. We find that the crystal melts abruptly into a layered fluid along a density gradient parallel to the glass surface. In Sec. IV, we compare the 3D situation of Sec. III with the melting of a 2D layer of the identical colloid: by bringing a second smooth glass surface parallel and close to the first we create a single layer confined between the glass walls. The in-plane density of this layer is varied by changing the spacing between the plates. By inducing a shallow wedge between the plates we create a density gradient parallel to the glass comparable in magnitude to that of the three-dimensional case. As a function of in-plane sphere density we find a much more gradual melting transition in which there are separate divergences of translational and orientational order. In Sec. V we make a detailed comparison between these two melting experiments in which only the dimensionality of the sample is charged. We summarize the differences and similarities observed in the

crystals near melting, the fluids near freezing, and the intermediate region between the two phases. We compare our 2D melting results with our earlier measurements on a different colloid and those published by other groups. We also discuss some remaining open questions and directions for future experiments and analysis.

The goal of our study is the comparison by direct imaging of a 3D and a 2D situation in which the sample and smooth walls are otherwise identical and only the dimensionality of the sample changes. We will concentrate in this paper on the imaging of the first layer of the 3D sample next to the glass surface and postpone the detailed study of the density profile of the 3D sample perpendicular to the glass and our conclusions from this experiment on the possible melting mechanism in 3D for future publications.

II. EXPERIMENTAL

A. Sample cell and handling

Details of the colloid handling procedures, construction, and arrangement of the cell used to contain the colloid are given elsewhere.[27,29] A gold and epoxy plated copper cell contains the colloid. In the center of the cell on the top and the bottom are two opposing parallel glass windows, the distance between which can be changed from 0 to 0.1 cm by the use of three differential micrometers. The viewing region between the windows is the thin region of the cell. It is surrounded by several 70-μm mesh nylon bags containing H and OH ion-exchange resin. The top cell window is an optical flat onto which is glued a smooth cover slip facing the colloid. The bottom cell window is a single 150-μm-thick cover slip epoxied into a flange. Cover slips are used because they have no scratches on the 0.1-μm scale which tend to align the colloid as have optical flats. Surrounding this thin region is a 100-cc annulus of 3D crystalline colloid in intimate contact with both the ion-exchange resin and the thin region. Because the cover slip glued on the top window is smaller in diameter than the viewing region we can easily equilibrate and image a thick sample out from under the top cover slip and a thin sample directly under the cover slip. These thick and thin regions are in direct contact with each other and can be imaged at the same time.

The cell is sealed from contact with air to avoid contamination with carbonate ions and regulated to a temperature of 29 ± 0.1 °C to minimize differential thermal expansion effects. When the distance between the two opposing cover slips is greater than ~10 μm the cell is opened to atmospheric pressure via a 3-m-long vertical tube continuously flushed from the top with Ar gas to minimize the bowing of the bottom cell window due to atmospheric pressure fluctuations.

Varying the system temperature is not particularly useful in these colloid imaging experiments. In general, raising the system temperature results in an unknown and uncontrolled influx of additional screening charges into the solution due to the activated nature of the ionic dissociation constants of the walls of the container, the spheres themselves, or anything else in contact with the solution. For this reason, all of our experiments are carried out at a few degrees above room temperature with the colloid in direct contact with ion-exchange resin. The resin is used in order to minimize extra salt concentrations, unknown ion gradients, and accompanying large unknown changes in effective Coulomb screening lengths. Sphere density is used as the experimental variable as it is intrinsically more controllable.

In order to obtain a reproducible, gradual change of 3D sphere density in our cell without an externally imposed osmotic pressure change we make use of the very slow diffusion coefficient of the spheres in water compared to that of the screening ions, at least five orders of magnitude faster. If we impose a density gradient of the colloid in the cell in our filling procedure, the counterions will come into equilibration with the colloidal sphere density gradient within about a day, whereas the density gradient of the spheres would take about a year to disappear. In the study of 3D melting near a glass wall we probe along existing 3D density gradients parallel to the wall after about a month's equilibration after the cell is filled. In the 2D experiment we impose a density gradient in the single colloid layer that is comparable to that of the 3D case by creating a very small wedge angle between the two confining glass plates.[19]

B. Digital video microscopy

The 3D crystal grows with the highest density face ([111] for fcc) at the smooth glass surface.[30] Once the colloid has equilibrated for a month in the cell with an imposed density gradient along y, it is probed by imaging through the bottom window in the x-y plane a small volume of size $\Delta x\times\Delta y\times\Delta z=59\times46\times0.4$ μm^3 or $\sim45\times35\times1$ spheres. The imaging is done in the thin viewing region with the 140X, numerical aperture 1.3, oil immersion objective of an inverted Reichart optical microscope. An incoherent Xe arc lamp with three ir-uv blocking filters and a broad blue-green notch filter is used as the excitation source using Kohler illumination. The smaller dimension Δy of the digitized area in the plane of the window is set parallel to the macroscopic density gradient along y. The extent of the sample with an in-plane density n within $\pm1\%$ is at least 35×450 spheres. The depth of focus of the objective is ±0.2 μm and the penetration depth of the light in the z direction, determined by the exponential loss of image contrast as one steps the focus through well ordered crystalline layers,[29] is roughly 7 layers (~7 μm). The imaging optics are exactly the same for the 2D experiment.

We use a standard video camera and video frame grabber[31] to digitize several snapshots at several positions along the imposed density gradient in the cell. The snapshots are separated by a time interval of 0.05 sec, sufficiently short that we can easily resolve the movement of individual spheres.[27] In this paper we will concentrate on the real-space imaging of the first layer of spheres parallel to the glass surface. We have previously shown[29] that a 3D colloidal fluid is layered near a smooth surface with a density profile very similar to its first layer in-plane pair correlation function. The width of the first

layer is quite sharp in the fluid near freezing and our task of imaging the spheres in the fluid is simplified considerably by this boundary condition.

C. Data analysis

The centers of spheres are located digitally to ± 1 pixel accuracy as described in detail elsewhere.[29] The particle-center locations in snapshots are used to determine in-plane density, translational correlation functions, structure factors, and orientational correlation functions making use of fast Fourier transforms and an array processor as described in Murray and Wenk.[27] The in-plane density n is expressed in reduced units of inverse particle diameters squared. The pair correlation function $g(r)$ is standard[32] and we use for the orientational correlation function the quantity

$$g_6(r)=\frac{\left[\sum_0^M \Psi_0^*(r')\Psi_6(r'-r)dr'\right]}{g_b(r)}, \quad (1)$$

where $\Psi(r)=e^{-i6\theta(r)}$ is the bond orientational order parameter at the center of the bond at r making angle θ with respect to the x axis, M is the total number of bonds in the field, the parentheses imply an azimuthal average, and $g_b(r)$ is the bond center pair correlation function. For the translational order parameter correlational function $g_G(r)$ we use a slightly modified form[6]

$$g_G(r)=\frac{\left[\sum_0^N \Psi_G^*(r')\Psi_G(r'-r)dr'\right]}{g(r)}, \quad (2)$$

where the translational order parameter at the particle center r is $\Psi_G(r)=e^{-iGr}$, G is a reciprocal lattice vector, N is the total number of particles in the field, the parentheses imply and azimuthal average, and $g(r)$ is the pair correlation function of particle centers.

In order to obtain limiting thermodynamic behavior of these functions and thus the limiting spatial and temporal behavior, we would need to average our correlation functions over many (10^2–10^3) images displaced from each other either in space by a distance larger than the correlation length or in time by an interval longer than the correlation time. Also we would need to compute the functions over several decades in distance (not presently available in our images but existing in our system) in order to determine the difference between exponential and algebraic envelopes to the curves. For this reason we do not wish to emphasize in detail the fits to exponents to the calculated correlation functions for a single image. However, trends in the data are certainly apparent and meaningful.

In order to categorize the topological defects in the images, we determine the nearest neighbors in each snapshot by performing a Voronoi polyhedron analysis on the positions of all sphere centers.[33] This procedure uniquely locates the disclinations or nonsixfold coordinated spheres in the layer. We make use of a fast sweepline algorithm invented by Fortune[34] to do the Voronoi analysis and to compute the Delaunay triangulation of each image of sphere centers. The Delaunay triangulation is the dual of the Voronoi polyhedra for a set of points in the plane and is a unique triangulation that maximizes the minimum angles of all triangles.[33] We use this to determine and plot the nearest-neighbor bonds of each sphere in an image and to obtain disclination statistics. Once the particle centers are located in a series of N snapshots spaced apart by an interval δt, we use a straightforward algorithm to link each particle with itself in successive frames[27] and use this to plot the individual particle trajectories for the time $N\delta t$.

III. RESULTS—3D

We made seven 3D melting runs over a period of two months after first waiting a month for the screening ions to equilibrate after the insertion of a new colloid to the cell. In these runs we took advantage of naturally occurring density gradients parallel to the glass windows a month after the cell was filled and shaken from side to side. We will only discuss the imaging of the first layer next to the glass here postponing the detailed description of the density profile of the system in the z direction, perpendicular to the glass wall, for future publications. We found the changes in in-plane density from the crystal to the fluid to be consistent from run to run at about 5% but the lowest density crystal just before melting varied from run to run by as much as 5% in in-plane density. This indicates that the screening length is not constant in vastly different regions of the 2-cm diameter viewing region of the cell. All of the 3D runs exhibited an abrupt interface. We will discuss the results of one of these runs here. In this run we digitized five images separated by 0.05 sec at each of nine different locations along the direction y of the density gradient. A particle in the dense fluid would diffuse about $0.2a$ in ~ 0.1 sec, if the diffusion in the solvent were unhindered by collisions.[27] The first and last images are separated by 290 μm but typically the centers of successive digitized images are separated by 20 μm along y in the transition region so that there is significant overlap between the fields of successive images, as will be evident from the figures.

A. Experimental geometry-density gradient along smooth interface

A blow up schematic of the 3D sample geometry in the y-z plane is depicted in Fig. 1 in which is also shown a typical instantaneous position of the crystal-melt interface and the relative size of the digitized image along y. The total thickness t of the colloid for these runs was adjusted by opening the cell outside of the very thin region used for the 2D experiment to 500 μm so that $t \sim 500$ layers along z. The 3D colloid runs were performed at the same time—within days—as the 2D runs separated by ~ 0.3–0.5 cm from the central 2D region. As mentioned earlier, the [111] hexagonal face of the fcc crystal nucleates at the highly charged glass surface. Actually, we find the crystal does not favor fcc ($ABCABC\ldots$) stacking until it has attained a thickness of $\sim$ten layers. Between one and ten layers the crystal appears to have a

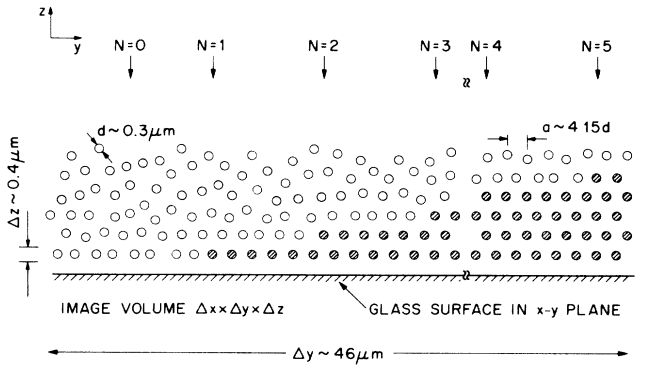

FIG. 1. Geometry (not to scale) of the 3D imaging experiment. The smooth glass surface is in the x-y plane with the imposed sphere density gradient along y. Here a schematic cross section of the instantaneous 3D crystal-fluid interface is depicted in the y-z plane. Solid circles represent ordered spheres and open circles represent those that are disordered from their crystalline positions. The intersection of the imaging volume $\delta x \times \delta y \times \delta z = 59 \times 46 \times 0.4$ μm in the y-z plane containing roughly 1800 spheres in the first layer of colloid next to the glass wall is also marked. The N-layer crystal nucleates at the glass wall ($N=1$) and grows in thickness to $N=5$ layers on the right-hand side of an image containing the crystal-fluid interface in the first layer at left.

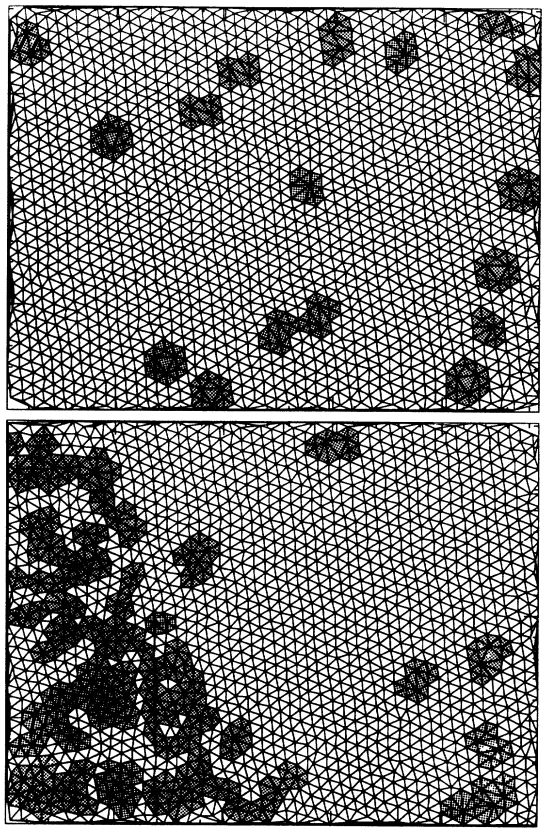

FIG. 2. Delaunay triangulations of snapshots containing instantaneous particle positions for the 3D run. The center of each particle in the image is at a vertex with nearest neighbor-bonds shown by the lines. Defects in the topology of the lattice, or particles that are not sixfold coordinated, are highlighted by having their near neighborhoods shaded. Tic marks on the borders of each snapshot are separated by 20 pixels, or 2.4 μm. Top (a) in-plane density $n=0.0599$ just into crystal; bottom (b) $n=0.0587$ just into intermediate region. Note the relatively sharp interface between order and disorder on the left-hand side of (b).

packing sequence closer to that of HCP ($ABAB\ldots$), often with a great deal of shear between layers and considerable stacking disorder. The triangular symmetry of the layers is on average maintained. From widths of truncated crystal diffraction rods observed with incident laser light along the [111] axis, projected onto a screen on the top window, we can set an upper limit of less than 1% for the possible density gradients that could exist in the z direction (perpendicular to the glass wall) on the crystal side of the melt interface. We observe in the crystal near melting a rather high fraction of $\sim 0.8\%$ hops of particles between the first and second layers within 0.05 sec.

We typically observe a rather steep and abrupt interface in this colloid in the y-z plane: a new crystalline layer grows in on top of the lower one roughly every 7–8 nearest-neighbor spacings farther from the interface in the layer just below, as depicted schematically in Fig. 1. The interface also appears rather flat on average in the x direction in the x-y plane although small wavelength fluctuations in this direction are large and we have not studied them carefully. These fluctuations cause an apparent tilt in the microscopic interface in the x-y plane in this run as will be evident from the figures. It is quite abrupt along y in the x-y plane as we will show in the following sections.

B. First layer: snapshots, trajectories, and defects

Delaunay triangulations for instantaneous particle configurations at various densities near melting, corresponding to center separations of 20 μm between images, are shown in Figs. 2 and 3. In these figures each particle center is represented by a vertex and the lines emanating from it are the bonds to its nearest neighbors. The nearest neighborhoods of nonsixfold coordinated spheres are shaded in order to reveal the instantaneous defect structure. The sharp melt interface is particularly evident in Figs. 2(b) and 3(a), with most of the defects clustered on the lower left-hand side of each image. In Fig. 4 are plotted the trajectories of all particles at the location corresponding to Fig. 2(b), for a duration of 0.2 sec. This figure also shows an abrupt boundary between fluidlike and solidlike regions. In Fig. 5 is plotted the percent crystal fraction of various snapshots taken through the transition region determined by eye from the images in Figs. 2–4. To within experimental accuracy we find the fraction of crystal to be linear in the transition region, implying an abrupt interface over several minutes duration.

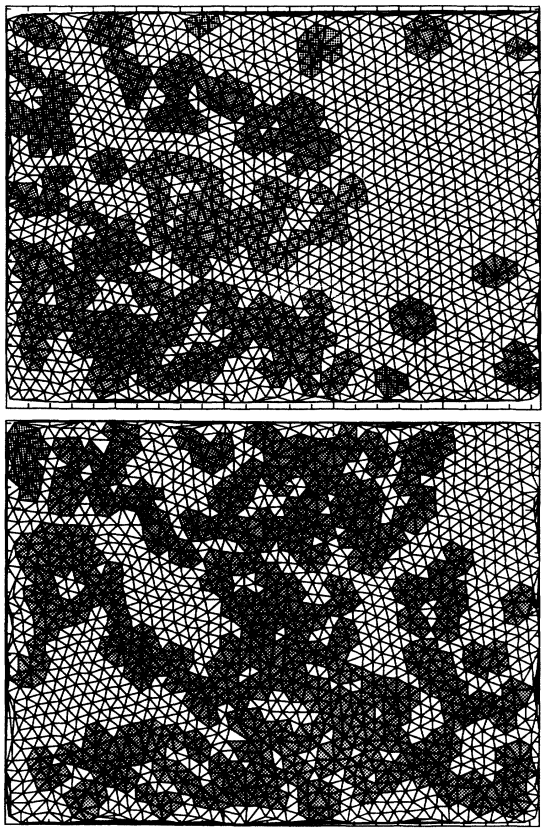

FIG. 3. Delaunay triangulations of snapshots containing instantaneous particle positions for the 3D run. The center of each particle in the image is at a vertex with nearest-neighbor bonds shown by the lines. Defects in the topology of the lattice, or particles that are not sixfold coordinated, are highlighted by having their near neighborhoods shaded. Tick marks on the borders of each snapshot are separated by 20 pixels, or 2.4 μm. Top (a) in-plane density $n=0.0578$ in the intermediate region; bottom (b) $n=0.0571$ lower-density intermediate region just before fluid. The sharp interface between order and disorder is still visible here.

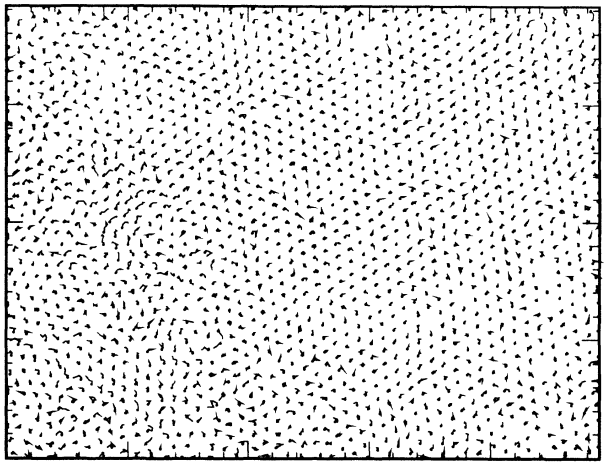

FIG. 4. Individual particle trajectories in five time steps separated by 0.05 sec for $n=0.0587$ in the 3D run in the intermediate density region very close to the crystal. The final positions of the particles are depicted by solid circles. On the right-hand side of the image the majority of particles oscillate about their equilibrium positions. Note the sharp interface at left between these movements characteristic of the crystal and more fluidlike trajectories at bottom left. Compare these trajectories with an instantaneous configuration of spheres at this density in Fig. 2(b).

1. *In-plane density in the first layer*

In Fig. 6 is plotted the average in-plane density n (in units of inverse diameters squared) determined by counting spheres in snapshots as a function of the image center location along y. In the figure the error bars in n are estimates of possible experimental errors due to problems counting spheres close to the image edges, while the error bars in y depict the size of the image, 45 μm, along y. The sharp changes of slope between the densities marked $n_a=0.0555$ and $n_b=0.0598$ in the figure are another indication of the abruptness of the melt interface. Also, not shown in the figure, the average densities in the "crystal" and "liquid" regions for $n_a<n<n_b$ are found to be very close to what is expected from extrapolations of the slopes of the crystal and liquid far from the interface, respectively.

2. *Static correlation functions in the first layer*

In Fig. 7 are plotted the static pair correlation functions $g(r)$ and the static orientational correlation functions $g_6(r)$ for a number of snapshots in the run. The translational correlation length ξ [determined from fits to $g(r)$ of an exponential decay envelope multiplied by the pair correlation function of a broadened perfect triangular crystal][27] is marked by arrows on both plots for each

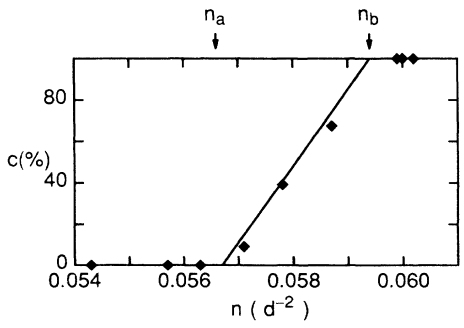

FIG. 5. Percent crystal fraction for the images in the 3D run at various densities obtained from observation of instantaneous defects and particle trajectories. The line from 0% at n_a to 100% at n_b is a guide to the eye but also a reasonable fit to the crystal fraction of each image. Estimates of errors are roughly the size of the plotted symbols.

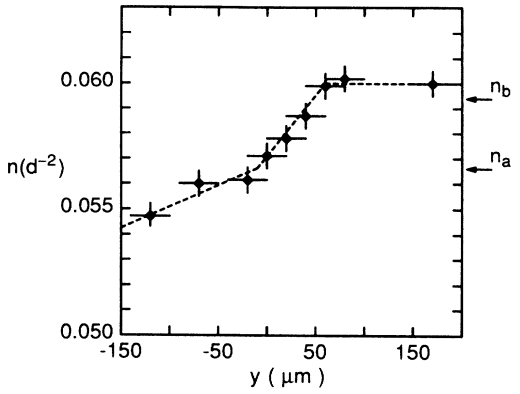

FIG. 6. In-plane density n vs position y along the density gradient for the 3D run. Error bars in y (abscissa) depict the extent of the digitized images while those in n (ordinate) depict an estimate of counting errors due to edge effects. Dashed lines are a guide to the eye. Note the sharp breaks in slope at n_a and n_b marking the extent of the intermediate region between crystal and fluid.

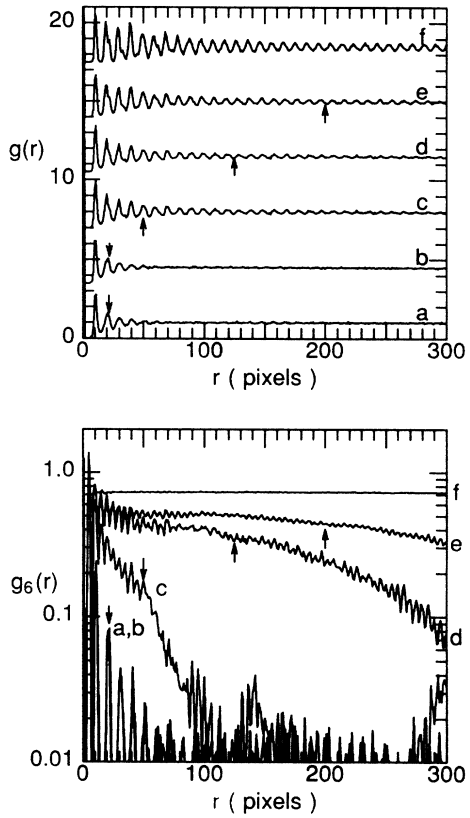

FIG. 7. Top: instantaneous pair correlation functions $g(r)$ for the 3D run. Successive curves at successive densities a–f are displaced upwards for clarity. Bottom: instantaneous orientational correlation functions $g_6(r)$ for the same densities as marked. These are not displaced vertically. The arrows for each curve mark the spatial correlation length ξ at that density determined by fitting $g(r)$ to an exponentially decaying envelope. The densities for the curves are as follows: (a) fluid at $n=0.0560$; (b) fluid at $n=0.0561$; (c) intermediate region at $n=0.0571$; (d) intermediate region at $n=0.0578$; (e) intermediate region at $n=0.0587$; (f) crystal at $n=0.0599$.

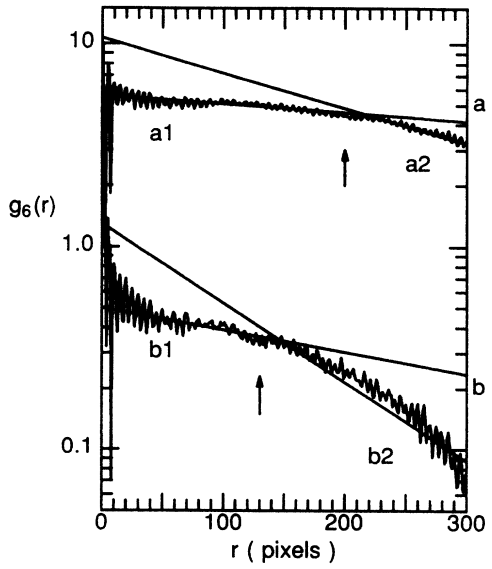

FIG. 8. Instantaneous orientational correlation functions $g_6(r)$ for two densities in the intermediate region for the 3D run. (a) top curve: $n=0.0587$; (b) bottom curve: $n=0.0578$. Curve (a) is displaced upwards by a multiplicative factor of 10 for clarity. The arrow for each curve represents the value of the translational correlation length ξ at each density. Note the sharp breaks in each curve very close to ξ. Curves a1 and a2 are exponential fits to the slope of curve (a) for $r<\xi$ and $r>\xi$, with decay lengths 4ξ and $\xi_6=1.0\xi$, respectively. Curves b1 and b2 are exponential fits to the slope of curve (b) for $r<\xi$ and $r>\xi$, with decay lengths 3.2ξ and $\xi_6=0.89\xi$, respectively.

density. This translational correlation length grows as a function of n. Of interest in these plots is the behavior of the orientational correlation function with n. For densities $n>n_b$ in the crystal it is constant. For densities $n<n_a$ in the fluid it decays exponentially fast with an orientational correlation length $\xi_6=\xi$. For $n_a<n<n_b$ in

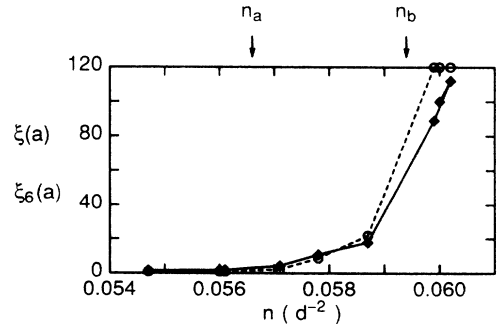

FIG. 9. Solid diamonds and solid lines: translational correlation length ξ in units of nearest-neighbor distances "a," for the 3D run, determined by fits to exponentially decaying envelopes of $g(r)$ calculated from instantaneous snapshots of particle positions at each density. Open circles and dashed line: orientational correlation length ξ_6 for the same images in the same units determined from exponential fits to $g_6(r)$ for $r>\xi$. The lines are a guide to the eye and the highest plotted points for ξ_6 are lower bounds. The extent of the intermediate region between crystal and fluid is marked by the arrows at n_a and n_b.

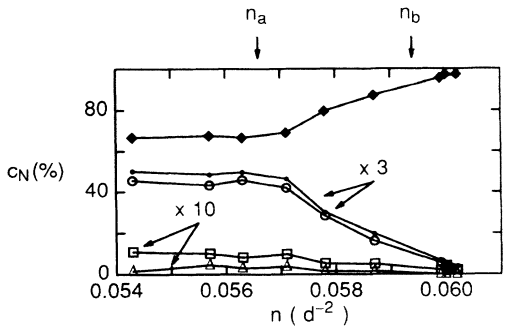

FIG. 10. Concentration c_N in percent of n-fold coordinated particles in instantaneous images in the 3D run vs density with $2<N<9$. Solid diamonds: $c_6\times1$ (ordered particles); small solid circles: $c_7\times3$; open circles: $c_5\times3$; open squares $c_8\times10$; open triangles: $c_3\times10$. The extent of the intermediate region between crystal and fluid is marked by the arrows at n_a and n_b.

the intermediate region there is a break in $g_6(r)$ which occurs at $r=\xi$. This is shown more clearly in Fig. 8, along with fits to exponential decays for both $r<\xi$ and $r>\xi$. For $r>\xi$ the exponential decay length ξ_6 is comparable to ξ. This is shown in Fig. 9, in which the two correlation lengths ξ and ξ_6 are plotted versus n. For $r<\xi$ in the density region $n_a<n<n_b$, the slower decay in space of $g_6(r)$ in Figs. 7 and 8 is a reflection of the crystalline portion at the right of each image.

3. *Defect statistics in the first layer*

In Fig. 10 are plotted the concentrations of N-fold-coordinated spheres for the 3D melting run versus density expressed as a percent of the total number of spheres and computed for the center 75% of each image to avoid edge effects. We will discuss these defect statistics and the arrangements of defects shown in Figs. 2 and 3 in comparison to those of the 2D run in Sec. V.

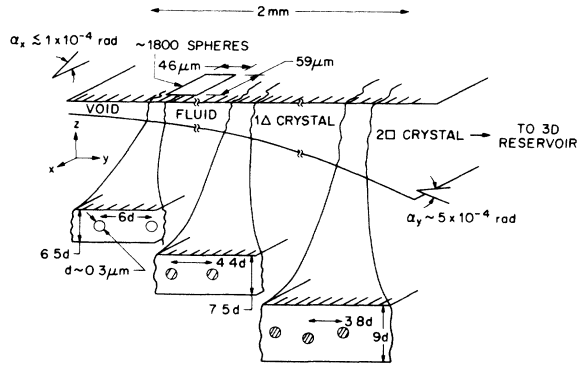

FIG. 11. Schematic of the experimental geometry for the 2D run (not to scale). The imposed density gradient of particles in the y direction is induced by a small wedge angle $\alpha_y\sim5\times10^{-4}$ radians between two smooth glass plates. The angle α_x along x is set to be as small as possible. The particles are confined rigidly in the x-y plane by the repulsive particle-wall potential until the plates are separated by ~9 diameters which is beyond the plate separation at melting of ~7.5 diameters. The imaging volume in the x-y plane is shown. It is centered in z at the focus on the 2D layer.

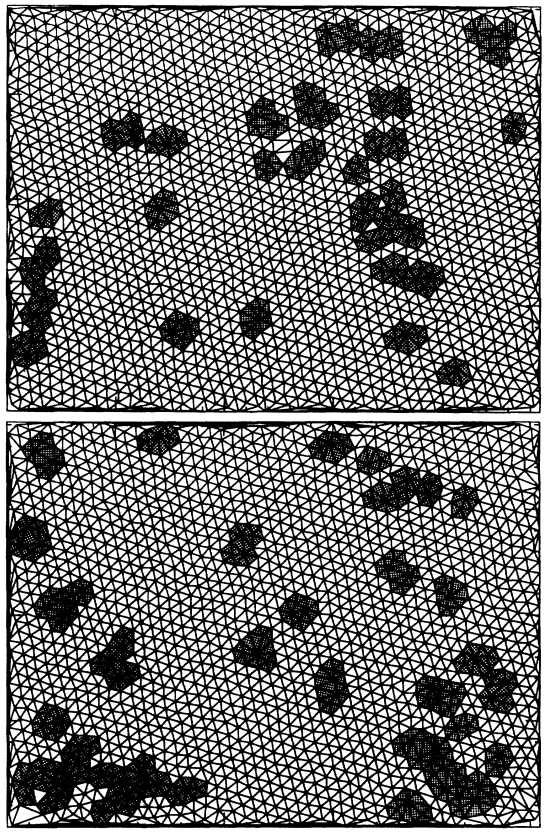

FIG. 12. Delaunay triangulations of snapshots containing instantaneous particle positions for the 2D run. The center of each particle in the image is at a vertex with nearest-neighbor bonds shown by the lines. Defects in the topology of the lattice, or particles that are not sixfold coordinated, are highlighted by having their near neighborhoods shaded. Tic marks on the borders of each snapshot are separated by 20 pixels, or 2.4 μm. Top (a) in-plane density $n=0.0606$ just into the crystal; Bottom (b) $n=0.0590$ just into the intermediate region. Compare the more gradual interface in 2D with the sharp transition in 3D of Fig. 2.

IV. RESULTS—2D

A. Experimental geometry-density gradient along wedge

In Fig. 11 is shown a blowup of the present experimental 2D geometry. The largest wedge angle between the glass walls (and therefore the major density gradient in the system) is along y. Melting of the 2D layer is observed at a nearest-neighbor sphere separation $a\sim4.4d$ and distance between the glass walls $t=7.5d$, considerably before any out-of-plane motion is measurable. We begin to measure out-of-plane motion at the ±0.05 μm level (±5% of the 3D vertical layer spacing along z) about 750 μm from the liquid-crystal boundary in y when $a=\sim3.8$ diameters, and $t=8.9$ diameters. Therefore, to good approximation the spheres are rigidly confined to

the plane through the 2D melting transition. The imposed density gradient along y due to the wedge corresponds to a change of sphere density of roughly $\pm 1\%$ per image (of size ~ 35 sphere separations) along the wedge. The wedge angle is better than a factor of 5 smaller in the x direction in the plane perpendicular to the wedge. The wedge topology is mapped out in detail with the optical microscope on a $\sim 50 \times 50$-μm grid both before and after an experimental run. The runs are taken at a position x_0 that corresponds to an inflection point in the plate separation (and sphere density) along x. Successive images are digitized at positions x_0,y for up to 15 different y values separated by 20–25 μm. During each run, which takes approximately one half hour, the wedge does not change to within our experimental accuracy of $\sim 1 \times 10^{-5}$ radians.

As the system is in direct contact with both thermal and particle reservoirs, constant chemical potential and temperature are maintained along the wedge in equilibrium. The major disadvantage in using a wedge geometry for this experiment is the imposed density gradient on the spheres in the direction of the wedge. This is the same geometry used in our earlier runs with a colloid with much different charge.[19,28] The density gradient would smear out a density jump associated with a first-order melting transition by our accuracy in measuring the density variation across an image. We have a gradient of similar magnitude in the 3D experiment described in the previous section and in that case have no difficulty observing a sharp density jump at the transition (see Fig. 8). The 2D crystal nearby would also serve as an orientation boundary condition for a possible hexatic phase in direct contact. The density gradient will produce on average one-half extra free dislocation per image with a Burgers vector perpendicular to the gradient. Of course, this is also the case for the three-dimensional density gradient and so is effectively identical in our "control" experiment.

The major advantage of the wedge geometry is that all phases can be equilibrated in parallel in the experiment. There are two time scales for equilibration: Initial equilibration of gradients in the screening ion density with the ion-exchange resin takes place in roughly a month. Afterwards, any small adjustment made in the wedge will drive the system out of equilibrium. In our experience, it then requires roughly 10–20 h to return to a consistent set of density of transitions, correlation lengths, and defect statistics.[27,28] In the present set of experiments we

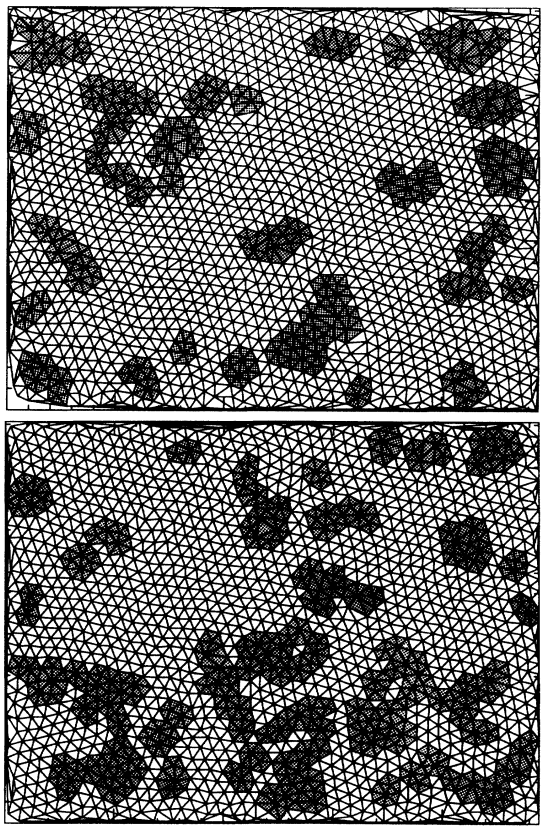

FIG. 13. Delaunay triangulations of snapshots containing instantaneous particle positions for the 2D run. The center of each particle in the image is at a vertex with nearest-neighbor bonds shown by the lines. Defects in the topology of the lattice, or particles that are not sixfold coordinated, are highlighted by having their near neighborhoods shaded. Tic marks on the borders of each snapshot are separated by 20 pixels, or 2.4 μm. Top (a) in-plane density $n = 0.0569$ in the intermediate region; bottom (b) $n = 0.0563$ lower-density intermediate region just before the fluid. Compare the 2D situation with that in 3D in Fig. 3.

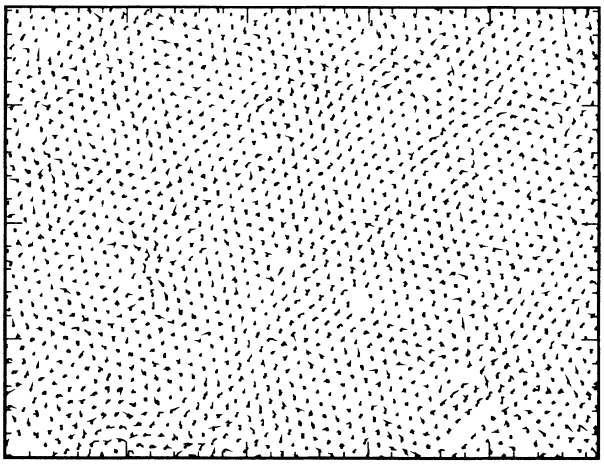

FIG. 14. Individual particle trajectories in five time steps separated by 0.05 sec for $n = 0.0590$ in the 2D run in the intermediate density region very close to the crystal. The final positions of the particles are depicted by solid circles. Here, the majority of particles oscillate about their equilibrium positions in relatively ordered regions and in-plane correlated hopping at the edges of the ordered regions takes place due to defect motion. Note the absence of an obvious sharp interface between clumped fluidlike motions and crystalline oscillations here in 2D in comparison with that of the 3D intermediate region of Fig. 4. Compare these trajectories with the instantaneous defect structure at this density in Fig. 12(b).

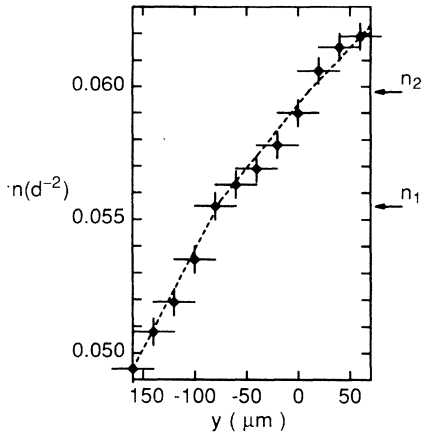

FIG. 15. In-plane density n vs position y along the density gradient for the 2D run. Error bars in y (abscissa) depict the extent of the digitized images while those in n (ordinate) depict an estimate of counting errors due to edge effects. Dashed lines are a guide to the eye. Note the much smaller breaks in slope at n_1 and n_2 marking the extent of the intermediate region between crystal and fluid in comparison to the 3D case of Fig. 6.

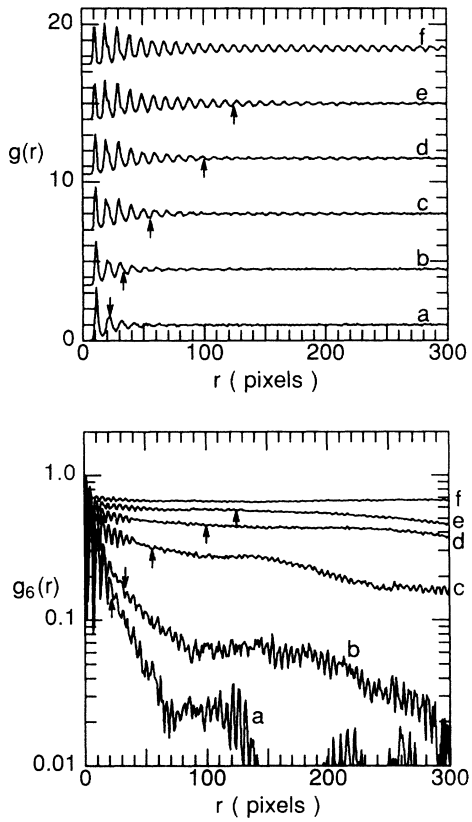

FIG. 16. Top: instantaneous pair correlation functions $g(r)$ for the 2D run. Successive curves at successive densities a–f are displaced upwards for clarity. Bottom: instantaneous orientational correlation functions $g_6(r)$ for the same densities as marked. These are not displaced vertically. The arrows for each curve mark the spatial correlation length ξ for each density determined by fitting $g(r)$ to an exponentially decaying envelope. The densities for the curves are as follows: (a) fluid at $n=0.0519$, (b) fluid at $n=0.0535$, (c) intermediate region at $n=0.0563$, (d) intermediate region at $n=0.0569$, (e) intermediate region at $n=0.0590$, (f) crystal at $n=0.0606$.

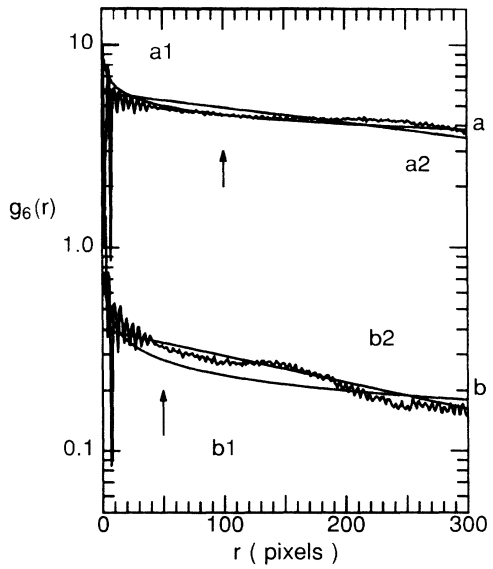

FIG. 17. Instantaneous orientational correlation functions $g_6(r)$ for two densities in the intermediate region for the 2D run. (a) top curve: $n=0.0569$; (b) bottom curve $n=0.0563$. Curve a is displaced upwards by a multiplicative factor of 10 for clarity. The arrow for each curve represents the value of the translational correlation length ξ at each density. Note that there are less obvious breaks in the curves at $r\sim\xi$ compared to the 3D case in Fig. 8. Curves a1 and a2 are algebraic and exponential fits to the curve (a) with exponent $\eta_6=0.15$ and orientational decay length $\xi_6=5.9\xi$, respectively. Curves b1 and b2 are algebraic and exponential fits to the curves (b) with exponent $\eta_6=0.25$ and orientational decay length $\xi_6=6.7\xi$, respectively.

made ten 2D melting runs over a period of four months all showing consistent densities of transition to within 2%. They were equilibrated for more than 24 h after an adjustment was made to the wedge. We will present the results from one of these runs. The range covered in y along the density gradient is 240 μm, and five successive frames separated by 0.05 sec were taken at 12 locations along the gradient separated by 20 μm.

B. Snapshots, trajectories, and defects

In Figs. 12 and 13 are shown the Delaunay triangulations of various snapshots for densities through the melting transition for the 2D run. These are to be contrasted with Figs. 2 and 3 for the 3D run. In Fig. 14 are plotted the trajectories of all the individual particles for the period 0.2 sec at a density $n=0.0590$ just below freezing corresponding to that of Fig. 4 for the 3D case. It is immediately obvious from these instantaneous particle positions and trajectories that the melting transition is much more gradual in 2D than it is in 3D, although it occurs at nearly the same in-plane density. There is no obvious two phase separation in the 2D case and the defects in the intermediate region—Figs. 12 and 13—are for the most part more isolated in small clusters and are not as

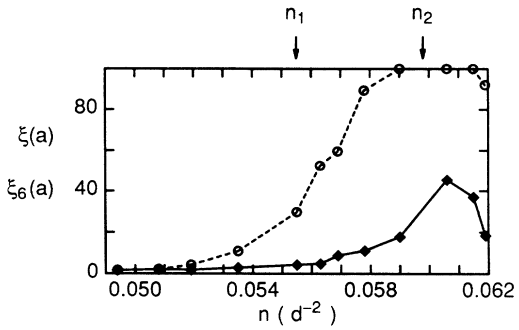

FIG. 18. Solid diamonds and solid lines: translational correlation length ξ in units of nearest-neighbor distances a for the 2D run determined by fits to exponentially decaying envelopes of $g(r)$ calculated from instantaneous snapshots of particle positions at each density. Open circles and dashed line: orientational correlation length ξ_6 for the same images in the same units determined from exponential fits to $g_6(r)$. The lines are a guide to the eye and the highest plotted points for ξ_6 are lower bounds. The extent of the intermediate region is defined here to be between n_1 and n_2 at which there are large increases in the orientational and translational correlation lengths, respectively. Compare this behavior with that of the 3D case in Fig. 9.

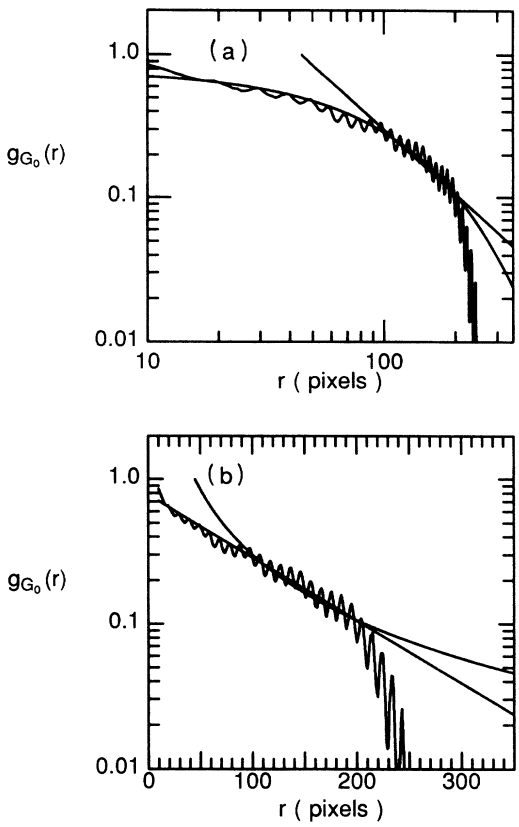

FIG. 19. Correlation function of the translational order parameter e^{-iGr} at $G=G_0$ the first reciprocal lattice vector for the 2D intermediate region just after melting at $n=0.0590$. Top (a) plotted on a log-log scale; bottom (b) plotted on a log scale in the ordinate only. The best fits to exponential (solid line) and algebraic (dashed line) decay are also shown. Neither curve fits the data for $r>200$ pixels, but the exponential decay is a better fit for $r<200$ pixels. Here the exponential decay length is 100 pixels, or $8.9a$, and the best fit exponent is $\eta=1.5$.

clumped together as in the lower left hand side "liquid" portion of the 3D snapshots in the intermediate region between all fluid and all crystal in Figs. 2 and 3. We will discuss the defect statistics and compare them to those of the 3D case in Sec. V.

1. *In-plane density*

The gradual nature of the transition in 2D is demonstrated by the very small changes of slope evident in the plot of in-plane density versus position along the gradient shown in Fig. 15. This behavior can be contrasted with the 3D case of Fig. 6. The 2D slope changes occur close to the densities n_1 and n_2 defined in the next section.

2. *Static correlation functions*

In Fig. 16 are plotted the instantaneous pair correlation functions $g(r)$ and the instantaneous orientational correlation function $g_6(r)$ for several images at representative densities in the 2D run near melting. These are to be contrasted with the analogous plots for the 3D run shown in Fig. 7. On the left hand column of Fig. 16 the trend with increasing density of the pair correlation $g(r)$ for the 2D case does not differ appreciably from that of the in-plane $g(r)$ for the 3D case in Fig. 7. On the figure the translational correlation length ξ is marked by arrows for each curve. This translational correlation length for 2D grows similarly to the in-plane translational correlation length in 3D except that the high density 2D fluid is more highly correlated than the 3D in-plane counterpart and the 2D crystal is less ordered in comparison to the 3D crystal. We will discuss this further in Sec. V. The orientational correlation functions, however, show a qualitatively different behavior as the dimensionality changes. Although $g_6(r)$ exhibits a few long wavelength oscillations due to the fluctuations in the ~ 1800 particle snapshot there is no obvious break in slope at ξ in 2D as there is in 3D (Fig. 8). The curves in 2D can be fit with a single exponential decay or algebraic decay as shown in Fig. 17. Of course, much more averaging over many uncorrelated snapshots and a longer distance range is needed to average out the long wavelength oscillations due to fluctuations[27] for a correct statistical limit fit to our curves.

In Fig. 18 are plotted the translational and orientational correlation lengths ξ and ξ_6 for the 2D run, where ξ and ξ_6 are defined in exactly the same way from $g(r)$ and $g_6(r)$, respectively, as in 3D. These correlation lengths can be compared directly to their 3D counterparts in Fig. 9. From the comparison of the translational and orientational correlation lengths fro the 2D and 3D experiments in these two figures it is clear that the 2D case does exhibit an intermediate region between fluid and crystal in which the orientational order is higher than the translational order. As in our earlier 2D experiments with a different colloid,[19,28] we use as the definitions for the transition densities n_1 and n_2 for the fluid-intermediate

boundary and the intermediate-crystal boundary, respectively, the midpoint densities between which ξ_6 and ξ increase dramatically. The falloff of ξ for $n > 0.061$ in the 2D compressed crystal is due to the beginnings of out-of-plane motion and incipient frustration caused by the nearby two layer crystal which has square symmetry in plane.[35]

We can make contact with the intermediate region of the 2D experiment and the hexatic phase of KTHNY theory providing some of the predictions of the theory can be tested. In particular, the hexatic phase should demonstrate exponential decay of the translational order and much slower algebraic decay of the orientational order. In Fig. 17, we show that a reasonable fit of algebraic decay to $g_6(r)$ just into the intermediate region at n_1 yields an exponent $\eta_6 \sim 0.25 \pm 0.05$ in good agreement with the KTHNY prediction of $\frac{1}{4}$, while $g_G(r)$ at this density, shown in Fig. 19, does appear to be best fit by fast exponential decay. However, at a density higher by 1%, just into the 2D crystal, we observe quite slow decay of translational order that can be fit with algebraic decay

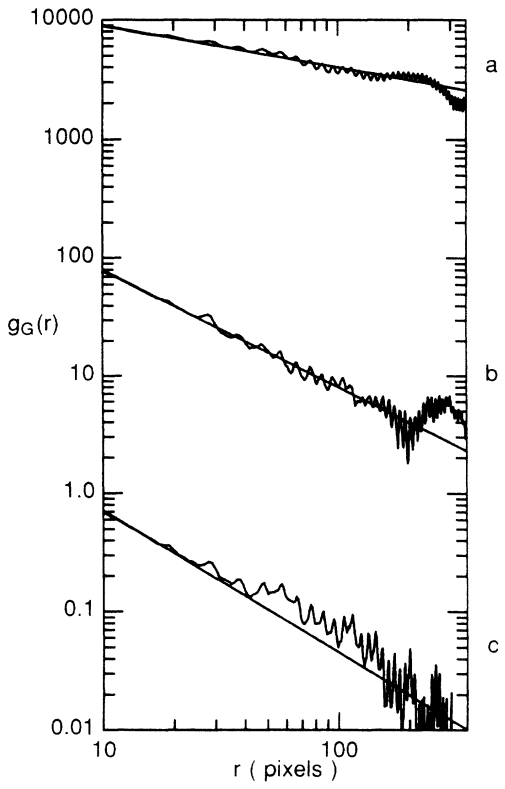

FIG. 20. Correlation function of the translational order parameter e^{-iGr} for the 2D crystal just before melting at $n = 0.0606$. Top (a) $G = G_0$, the first reciprocal lattice vector; center (b) $|G_1| = \sqrt{3} G_0$; bottom (c): $|G_2| = 2G_0$. The top and center curves are displaced vertically by multiplicative factors 10^4 and 10^2, respectively, for clarity. Also shown are plots of the best fit algebraic decay $r^{-\eta_G}$ for the separate data curves. From top to bottom the exponents are $\eta_0 = 0.3$, $\eta_1 = 1.0$, and $\eta_2 = 1.2$.

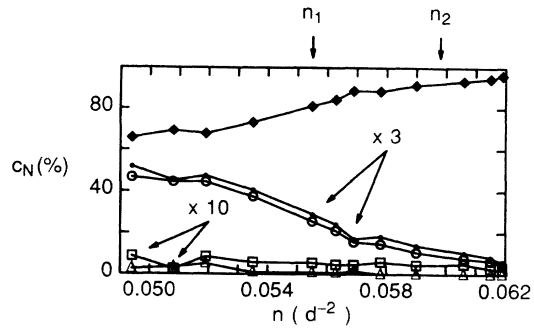

FIG. 21. Concentration c_N in percent of n-fold coordinated particles in instantaneous images in the 2D run vs density with $2 < N < 9$. Solid diamonds: $c_6 \times 1$ (ordered particles); small solid dots : $c_7 \times 3$; open circles: $c_5 \times 3$; open squares $c_8 \times 10$; open triangles: $c_3 \times 10$. The extent of the intermediate region between crystal and fluid is marked by the arrows at n_1 and n_2. Compare with the 3D case in Fig. 10.

$g_G(r) \sim r^{-\eta_G}$ as shown in Fig. 20. The Halperin-Nelson prediction[6,11] for η_G at melting is

$$\eta_G = \frac{|G|^2 a_0^2}{64} \pi^2 (1+\sigma)(3-\sigma) , \tag{3}$$

where $\sigma = \lambda_R / (\lambda_R + 2\mu_R)$ is the 2D Poisson's ratio of the crystal at the melting temperature, with λ_R and μ_R the Lame coefficients for the triangular lattice. Stability criteria for the solid impose limits on the 2D Poisson's ratio and thus the decay exponents η_G. For the limit of $\sigma = 1$ the largest $\eta_0 = \frac{1}{3}$ and for $\sigma = 0$ the smallest η_0 will be $\frac{1}{4}$. We find at $n \geq n_2$, $\eta_{G_0} = \eta_0 = 0.35 \pm 0.05$, $\eta_{G_1} = 1.0 \pm 0.05$, where $|G_1| = \sqrt{3} G_0$, and $\eta_{G_2} = 1.2 \pm 0.05$, where $|G_2| = 2G_0$. Best fit algebraic decay curves for these translational correlation functions in the crystal just above melting are plotted in Fig. 20. We find an excellent agreement with the KTHNY prediction for not only the value of η_0 at the limit of stability of the crystal, but also the G^2 dependence of η_G. Taking these three values together and using the expression for the predicted power law decay of Eq. 3, we obtain a "best fit" value for η_0 of 0.327 ± 0.025 just before melting. A best algebraic fit to $g(r)$ at this density just at melting yields a decay exponent of 0.1 ± 0.05, in excellent agreement with our earlier 2D melting runs using a different colloid[19] with implications that η_0 is also near $\frac{1}{3}$ for the earlier runs using lower charged colloid.

3. *Defect statistics*

In Fig. 21 are plotted the concentrations of N-fold coordinated spheres for the 2D melting run versus density expressed as a percent of the total number of spheres and computed for the center 75% of each image to avoid edge effects. These can be directly compared to those in the first layer of the 3D sample in Fig. 10. The first thing to note is that the 2D fluid is considerably more ordered than its 3D counterpart with over 80% sixfold coordination in 2D contrasted with 67% in the first 3D layer.

The 2D crystal is less ordered with 95% sixfold coordination at melting versus 98% in 3D. This is also obvious from the plots of correlation functions in Figs. 7 and 16.

V. CONCLUSIONS

A. Comparison of melting in 2 and 3D: this experiment

1. Crystal near melting

The first layer next to the glass wall of the 3D crystal near melting has triangular symmetry and is 98% sixfold coordinated with isolated small defect clusters—that are usually tightly bound dislocation pairs and triples. The translational correlation length, defined in a fit to an exponential decay to $g(r)$, is $\sim 90a$. There are $\sim 0.5\%$ vacancies, defined as vertices in the Delaunay triangulation with nearest neighborhoods that can accommodate an additional 0.8–1.2 particle. The region near melting ranges from one to five layers thick at the glass surface with FCC stacking preferred only after ten layers. There are $\sim 0.8\%$ hops to and from the first and second layers of crystal in 0.05 sec.

In comparison, the 2D crystal near melting also has triangular symmetry but the spheres are rigidly confined to the plane. It is less ordered than its 3D counterpart with 95% sixfold coordination and a translational correlation length of 30–40a. The defects also occur as isolated dislocation pairs and triples. There are roughly the same percentage of vacancies, $\sim 0.5\%$ as in the first layer of the 3D crystal. Because individual particles are rigidly confined to the plane and cannot take advantage of hopping to and from the second layer as in 3D, there is noticeably more correlated directional particle hopping in plane (see Figs. 4 and 14 for a comparison of particle trajectories just into the intermediate region). This correlated in-plane hopping is directly associated with defect motion as has been noted in our earlier experiments.[27,28,36] The spatial dependence of the instantaneous translational correlation function $g_G(r)$ is found to be consistent with algebraic decay $r^{-\eta_G}$. At melting, $\eta_0 \sim 0.33$ and $\eta_G \sim G^2$ which is in excellent agreement with KTHNY predictions.

2. Fluid near freezing

The 3D fluid near freezing is layered with density profile perpendicular to the wall very similar to its in-plane $g(r)$[29] and considerable exchange of particles between layers. The first layer at freezing is 67% sixfold coordinated with spatial correlation length $\sim 2a$ and defects highly clumped into large clusters that are linked together in such a way as to completely encircle small "ordered" regions—in other words–nearly grain-boundarylike. The defects are percolated across a region the size of our images in an instantaneous snapshot of particle configurations.

In contrast, the 2D fluid near freezing is rigidly confined to the plane and so still exhibits correlated directional particle hopping[27,36] as observed at higher density. It is much more ordered than its 3D counterpart: 80% sixfold coordinated with a spatial correlation length of $\sim 4a$ at freezing. The defects are clustered into strings which are percolated across the image in a snapshot of particle locations. However, the "ordered" regions in an instantaneous configuration are larger ($\sim 4a$) than their 3D counterparts.

3. Intermediate region

In the 3D system, there is a clear change of slope in the density versus position along the gradient at two average densities defining the intermediate region between fluid and crystal: $n_a < n < n_b$. The extent of the region $(n_b - n_a)/n_b \sim 5\%$. The intermediate region exhibits clear phase separation with two phases with densities very close to the extrapolated values for the crystal and fluid. The trajectories and defects in the two regions resemble those in the two phases mentioned above. The translational correlation length ξ varies between ~ 5 and $18a$ in this region. The orientational correlation function has a definite change in slope at $r = \xi$. For $r > \xi$, the orientational correlation length $\xi_6 = \xi$.

In contrast, for the 2D intermediate region $n_1 < n < n_2$ the change of slope in density versus position along the gradient is much less obvious than in 3D. The extent of the region is larger in density $(n_2 - n_1)/n_2 \sim 8\%$. There is also no obvious phase separation in the instantaneous snapshots of particle locations or their trajectories compared to 3D. The defects are clustered mostly into strings which are still isolated from each other for the most part. The string length grows as the density is lowered from the crystal at n_2 to the fluid at n_1. These strings percolate across the image very close to the fluid boundary at $n = n_1$. The defect clusters occasionally have a net Burgers vector but are more often composed of paired dislocations. The incidence of unpaired dislocations, or defect clusters with net Burgers vector that is not equal and opposite to any within the image, increases gradually by roughly an order of magnitude as the density is lowered within the intermediate region. More precise numbers must await more averaging over many images to obtain better statistics. The translational correlation length ξ varies from 4 to $18a$ similar to the 3D case. The orientational correlation function $g_6(r)$ does not exhibit a sharp break at $r = \xi$ but does oscillate slowly in these instantaneous configurations. If one smoothes out the oscillations, $g_6(r)$ is fit moderately well either to a slow algebraic decay with exponent varying from -0.25 to -0.05 or an exponential decay with correlation length varying from 10 to $200a$ as n varies from n_1 to n_2.

B. Comparison of this 2D run to other 2D melting runs in wedge geometry

In comparison to our seven earlier 2D melting runs in wedge geometry using colloidal spheres with identical diameter but lower charge,[19,27,28,36] we observe in this new

2D experiment remarkable consistency in the behavior of $g(r)$, $g_6(r)$, the translational, and orientational correlation lengths and also the defect configurations and statistics in instantaneous images as the density is varied from the fluid through the intermediate phase and on into the crystal. Of course, the densities of transition n_1 and n_2 are in this new set of runs about a factor of 3 smaller. For the higher charged colloid with a larger screening parameter in the present experiments, the extent of the intermediate region is about a factor of two larger (8% in density versus 4% in density for the earlier runs). This allows us to obtain better density resolution and relatively smaller gradients across the images in the present experiments. For both sets of experiments, our fits to algebraic decay for the orientational correlation function are in good agreement with the decay exponent $\eta_6 \sim 0.25$ at the intermediate region-fluid boundary. For the new experiments, we calculated the translational correlation function $g_G(r)$ in the crystal just at melting and obtained excellent agreement with the KTHNY prediction of algebraic decay with power $\eta_G \sim G^2$, and a value of $\eta_0 \sim \frac{1}{3}$ within experimental accuracy. If we fit the pair correlation function with an algebraic decay, we obtain an exponent at melting of 0.1 ± 0.05 for both colloids with the implication that both crystals become unstable at η_0 near one third.

Tang *et al.*[22] have performed an isothermal expansion experiment using charged colloidal spheres of diameter 1 μm between smooth glass plates. Depending on initial plate separation, they find melting at $a \sim 4$–$6d$ in two runs in which the plates were separated at 0.7 and 3.5 μm/min. The larger size of their spheres enables them to obtain a smaller density gradient in their images (also about 2000 spheres at melting) but limits the ratio of screening length to diameter or the screening parameter $\Lambda = a/\lambda$ to a considerably larger value compared to those of our two experiments. This comes about because the largest screening length λ one can obtain at room temperature in water is 0.7 μm due to H-OH dissociation equilibrium. If we take this limiting screening length for their experiment—clearly a gross overestimate—then their screening parameter is $\Lambda \gg 6$–9 for their two runs. This can be compared to estimates of our screening parameter: for this run $\Lambda \sim 3$ and $\Lambda \sim 3.5$ for our earlier experiments. The implications of this may be that the 1-μm spheres of Tang *et al.* are closer to the hard sphere limit in comparison to our 0.3-μm spheres which have a longer-range interaction potential. This is probably relevant to the driving mechanism for melting in the two systems as we see a factor of 2 increase in the extent of the intermediate region between our two experiments at $\Lambda = 3$ and $\Lambda = 3.5$.

As Tang *et al.* scan density with time in their experiments, they have an opportunity to watch defects evolve in time in the same region of the sample as the density is driven through melting. This is in contrast to our method of effectively maintaining ~ 10 slightly different density samples along our wedge in equilibrium measuring defect statistics and other things of interest for all samples in parallel. If one obtains good statistics in either experiment, the system were in thermodynamic equilibrium, and the wedge angle and the rate of separation of the plates were small, the methods should in principle produce identical answers as to the nature of the defects and melting on identical samples.

The major drawbacks to the two experiments are different: for the wedge a density gradient will always exist. This gradient could in principle round off any sharp first-order transition and also will by necessity add a small free-dislocation density background in the crystal. It is unclear to what extent the boundary conditions (densities differing by about 20% of the density difference between crystal and isotropic fluid on opposing sides of each separate ~ 35 particle image) will affect the nature of melting. It is hard to believe that this boundary condition will drive a more continuous KTHNY phase transition in the same manner as a sixfold oriented substrate.[6,11,24] As to whether the rounding effects will be severe enough to completely obliterate any signature of a first-order phase transition, we have a counterexample in the 3D experiment described in this paper.

For the expansion experiment, one has to worry about whether the expansion is really adiabatic or whether the system is being driven out of equilibrium. This could be important as we find[27,28,36] a mechanical equilibration time of ~ 10–20 h for our system which is roughly the time needed for a dislocation to climb over a correlation length near melting.[11] This is considerably longer than the 20 min–7 h period over which Tang *et al.* swept the entire density range from high-density crystal to low-density fluid. One might expect that the equilibration times for the two experiments scale to first order like the Stokes diffusion coefficient for the spheres $\sim 1/d$ so that the equilibration times for 1-μm spheres could be as long as several days.

Tang *et al.* observe in their experiment using isothermal expansion of a 2D layer of 1-μm diameter spheres a similar behavior in $g(r)$ and $g_6(r)$ to that shown in Fig. 16. They also observe between 80% and 96% sixfold coordination in the intermediate region that has longer-range orientational order than translational order in their experiment. By fits to these correlation functions they obtain estimates for η_6 at the intermediate-fluid boundary very close to $\frac{1}{4}$. During their sample expansion, they observe only minute changes of slope in the density with time as the system passes through the intermediate region boundaries. These observations are in excellent agreement with both our 2D melting experiments, and also consistent with KTHNY predictions for melting. The extent of their intermediate region varies with expansion time but is roughly 10% in density for their slow expansion run.

However, the results of our 2D experiments are in disagreement in several important respects. First, the translational correlation length of their crystal just after freezing is very small $\sim 8a$ (in comparison to that in our experiments of $\sim 30a$) and hangs at that value during expansion for $\sim 30\%$ variation in density. Second, their defect distribution in the intermediate region appears to be more clumped and less uniformly distributed than ours. They interpret their results in terms of a first-order grain-boundary driven transition with an intermediate

two phase region that curiously exhibits many of the predicted properties of a hexatic. A similar argument has recently been made about the results of big simulations of over 10^4 2D Lennard-Jones particles:[37] that somehow the two phase region in 2D exhibits a novel possibly fractally interconnected structure that is inhomogeneous down to the scale of an interparticle spacing yet contains an orientational transition that is quite KTHNY-like. The argument that the melting transition is first order in the simulations is based on phase boundaries determined by free-energy expansions for much smaller 2D Lennard-Jones systems.

Tang *et al.* argue that the transition they observe must not be consistent with KTHNY as (i) they observe small grain-boundarylike structures and defect clumping that resembles two phase coexistence in the intermediate region, and (ii) they never observe directly unbinding of dislocation pairs or disclination pairs. Instead they see a complicated structure of highly clumped disclinations with the number of disclinations increasing roughly linearly as density is increased through the intermediate region. We have a difficult time identifying grain-boundarylike loops in the high-density intermediate region of either of our two different colloids in any of our 17 different experimental runs (for example see Figs. 12 and 13), so this may be a distinct difference between our experiments and those of Tang *et al.* However, we believe that the renormalization group picture of the KTHNY theory cannot be taken too literally when one examines the microscopic defects of a system.

The renormalized defects that eventually unbind due to screening by intervening overlapping defect pairs are theoretically at infinite distance scales. If one could define an effective renormalized Burgers vector (or disclinicity) in a real experiment on a set of expanding distance scales, then one may then perhaps hope to see these large distance scale objects gradually unbinding as the system undergoes two separate Kosterlitz-Thouless transitions. While one observes the microscopic defects of the system, however, one observes all of the intervening dislocation pairs that are renormalized out of the KTHNY theory. As it is favorable energetically for these dislocations (and disclinations) to bind together[11] and perhaps even arrange into arrays,[8] it can be expected that the microscopic arrangement will be quite complicated, overlapping, and clumped. The exact microscopic arrangement of defects also may differ depending on microscopic details such as the ratio of defect core energies compared to interaction energies in the system.[8,10] If this ratio favors grain-boundary formation before the KTHNY dislocation pair unbinding can take place[8] then a first-order transition may intervene. But the resulting first-order transition and the two-phase region may be greatly affected by the nearby Kosterlitz-Thouless transition.[37] One might hope to learn something about defect pair unbinding on average in a statistical sense by making a statistical study of the microscopic defects.[36] We believe the best method of ascertaining whether a KTHNY melting transition occurs in a specific experiment is to measure as many universal predictions of the theory as possible including dynamics and temperature dependences of exponents. Nevertheless, the microscopic picture afforded by these imaging experiments is fascinating in its own right.

C. Summary

We observe separate divergences in orientational and translational correlations in our 2D experiment and a very gradual melting transition in contrast to the same system in 3D which exhibits an abrupt classical first order melting transition. The static exponents governing the algebraic decay of translational and orientational correlations at the two separate transitions in 2D are in excellent agreement with our earlier experiments and also the KTHNY predictions. The microscopic defect arrangements and particle trajectories are quite different in the 2D and 3D systems. While the microscopic defect arrangements in our 2D system are remarkably consistent with our earlier experiments using a different colloid through the melting transition at a vastly different density, they appear to be considerably less clumped into loop structures than those of Tang *et al.* in their expansion experiment.

The defects in our 2D experiments grow from isolated dislocation pairs and triples in the crystal into still longer three or four dislocation pair strings usually of unit width in the high-density intermediate region. As the particle density is lowered through the intermediate region, the strings grow in number and length and finally begin to touch each other just at the intermediate region-fluid boundary. In the high-density fluid, they resemble grain-boundarylike loops percolating through our images. The intermediate region between crystal and isotropic fluid is in our 2D experiments either a hexatic or a two-phase region greatly affected by the nearby KTHNY transition. Without thermodynamic measurements, measurements of the predicted values of the elastic constants near the transitions[11] and/or temperature dependences of exponents we cannot be absolutely certain that the system is undergoing a KTHNY transition. However, the defect arrangements mentioned above are inconsistent with a standard two-phase region similar to the one we observe in 3D and are quite consistent with what we would expect for a complicated microscopic picture of the hexatic.

Some open questions remain for future study. (i) Why are the defect densities and arrangements so similar throughout melting in the two 2D 0.3-μm sphere colloid experiments with different charge and screening parameters? (ii) Why are the disclination densities similar but the defect arrangements more clumped in the expansion experiment on 1-μm spheres of Tang *et al.*? (iii) What is the driving mechanism for the 3D melting we observe near a smooth wall? (iv) How does the layering of the 3D fluid near the wall change with increasing density near melting? (v) What does the freezing of the second or third or nth layer of the 3D crystal look like? (vi) How is melting or freezing affected in 2D or 3D by a modulated substrate? (vii) What are the thermodynamics and dynamics of the hexatic/intermediate regions? (viii) At

what values of relevant parameters does one observe KTHNY or first-order melting in real experimental 2D crystals? (ix) How does diffusion differ in a 2D fluid and a 3D layered fluid?

Clearly, digital imaging experiments on colloidal spheres have opened up a fascinating area of research to detailed study of such questions with excellent prospects of obtaining answers in the near future.

ACKNOWLEDGMENTS

We benefited from discussions with B. I. Halperin, D. R. Nelson, R. Pindak, F. A. Stillinger, W. van Saarloos, and J. R. Weeks. We are grateful for the gift of the sweepline Voronoi analysis source code from S. Fortune and also for early general digital imaging software support from R. Lee.

[1]B. J. Alder and T. E. Wainwright, J. Chem. Phys. **27**, 1209 (1957).

[2]D. Chandler, J. D. Weeks, and H. C. Anderson, Science **220**, 787 (1983).

[3]J. P Hansen and L. Verlet, Phys. Rev. **184**, 150 (1969).

[4]F. A. Lindemann, Z. Phys. **11**, 609 (1910).

[5]P. M. Platzman and H. Fukuyama, Solid State Commun. **15**, 677 (1974).

[6]J. M. Kosterlitz and D. Thouless, J. Phys. C **6**, 1181 (1973); B. I. Halperin and D. Nelson, Phys. Rev. Lett. **41**, 121 (1978); D. Nelson and B. I. Halperin, Phys. Rev. B **19**, 2457 (1979); A. P. Young, Phys. Rev. B **19**, 1855 (1979).

[7]H. Kleinert, Phys. Lett. A **95**, 381 (1983).

[8]S. T. Chui, Phys. Rev. B **28**, 167 (1983).

[9]T. V. Ramakrishnan and M. Yusoff, Phys. Rev. B **19**, 2775 (1979).

[10]An excellent recent review is given by K. J. Strandburg, Rev. Mod. Phys. **60**, 161 (1988).

[11]D. R. Nelson, in *Phase Transitions and Critical Phenomena,* Vol. 7, edited by C. Domb and J. L. Lebowitz (Academic, London, 1983), p. 1.

[12]R. J. Birgeneau and J. D. Litster, J. Phys. (Paris) Lett. **39**, 1399 (1978).

[13]M. Cheng, J. T. Ho, S. W. Hiu, and R. Pindak, Phys. Rev. Lett. **60**, 862 (1988).

[14]P. Pieranski, Contemp. Phys. **24**, 25 (1983).

[15]A. Homola and R. O. James, J. Colloid Interface Sci. **59**, 123 (1977).

[16]W. Hess and R. Klein, Adv. Phys. **32**, 173 (1983).

[17]E. B. Sirota, H. D. Ou-Yang, S. K. Sinha, P. M. Chaikin, J. D. Axe, and Y. Fujii, Phys. Rev. Lett. **62**, 1524 (1989).

[18]M. O. Robbins, K. Kremer, and G. Grest, J. Chem. Phys. **88**, 3286 (1988).

[19]C. A. Murray and D. H. Van Winkle, Phys. Rev. Lett. **58**, 1200 (1988).

[20]P. Pieranski, L. Strzelecki, and B. Pansu, Phys. Rev. Lett. **50**, 900 (1983).

[21]N. A. Clark, B. J. Ackerson, and A. J. Hurd, Phys. Rev. Lett. **50**, 1459 (1983).

[22]Y. A. Tang, A. J. Armstrong, R. C. Mockler, and W. J. O'Sullivan, Phys. Rev. Lett. **62**, 2401 (1989); Y. A. Tang, A. J. Armstrong, R. C. Mocker, and W. J. O'Sullivan (unpublished).

[23]A. J. Armstrong, R. C. Mockler, and W. J. O'Sullivan, J. Phys. Condens. Mat. **1**, 1707 (1989).

[24]G. Aeppli and R. Bruinsma, Phys. Rev. Lett. **53**, 2133 (1984).

[25]R. Pandit, M. Schick, and M. Wortis, Phys. Rev. B **26**, 5112 (1982).

[26]J. Z. Larese, L. Passell, A. D. Heidemann, D. Richter, and J.

[27]C. A. Murray and R. A. Wenk (unpublished).

[28]C. A. Murray, D. H. Van Winkle, and R. A. Wenk, Phase Transitions **21**, 93 (1990).

[29]D. H. Van Winkle and C. A. Murray, J. Chem. Phys. **89**, 3885 (1988).

[30]N. A. Clark, A. J. Hurd, and B. J. Ackerson, Nature **281**, 57 (1979).

[31]Recognition Technology, Inc., Holliston, MA 01746.

[32]J. P. Hansen and I. R. McDonald, *Theory of Simple Liquids* (Academic, London, 1986), Chap. 7.

[33]F. P. Preparata and M. L. Shamos, *Computational Geometry, an Introduction* (Springer-Verlag, New York, 1985).

[34]S. Fortune, Algorithmica **2**, 153 (1987).

[35]D. H. Van Winkle and C. A. Murray, Phys. Rev. A **34**, 562 (1986).

[36]C. A. Murray and R. A. Wenk, Phys. Rev. Lett. **62**, 1643 (1989).

[37]C. Udink and J. van der Elsken, Phys. Rev. B **35**, 279 (1987); C. Udink and D. Frenkel, *ibid.* **35**, 6933 (1987).

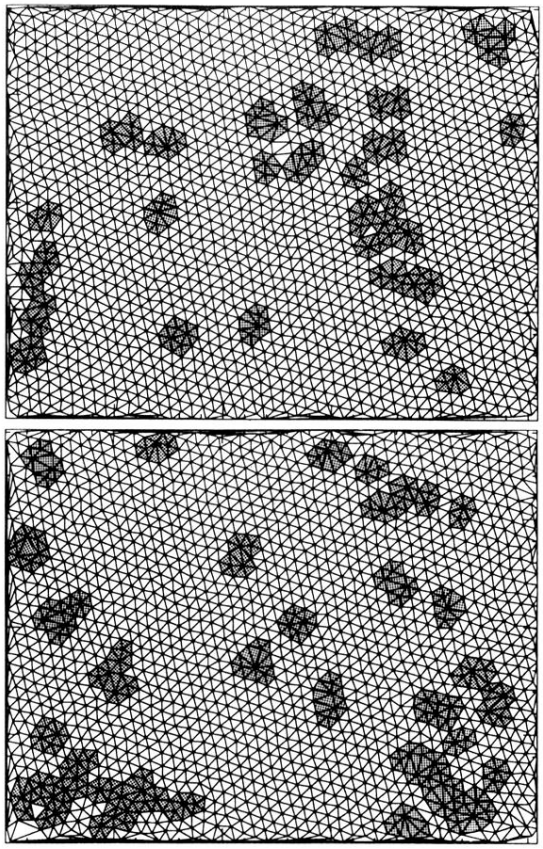

FIG. 12. Delaunay triangulations of snapshots containing instantaneous particle positions for the 2D run. The center of each particle in the image is at a vertex with nearest-neighbor bonds shown by the lines. Defects in the topology of the lattice, or particles that are not sixfold coordinated, are highlighted by having their near neighborhoods shaded. Tic marks on the borders of each snapshot are separated by 20 pixels, or 2.4 μm. Top (a) in-plane density $n = 0.0606$ just into the crystal; Bottom (b) $n = 0.0590$ just into the intermediate region. Compare the more gradual interface in 2D with the sharp transition in 3D of Fig. 2.

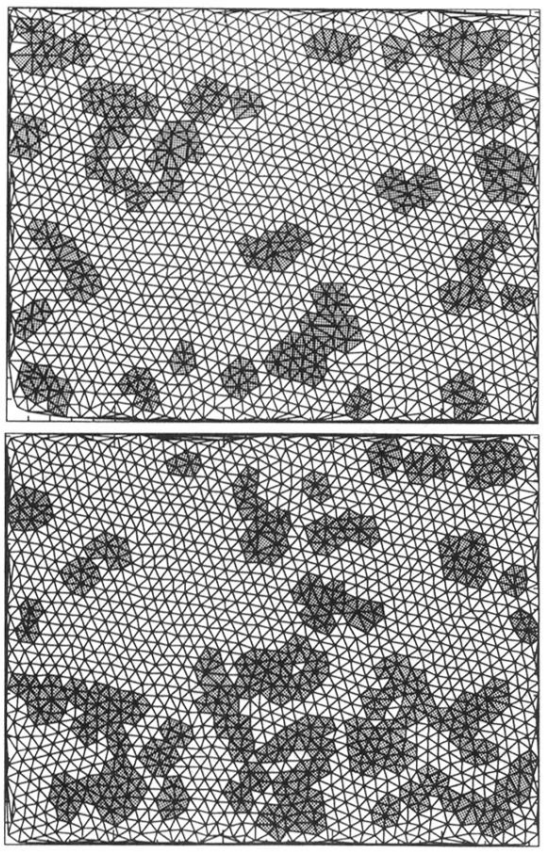

FIG. 13. Delaunay triangulations of snapshots containing instantaneous particle positions for the 2D run. The center of each particle in the image is at a vertex with nearest-neighbor bonds shown by the lines. Defects in the topology of the lattice, or particles that are not sixfold coordinated, are highlighted by having their near neighborhoods shaded. Tic marks on the borders of each snapshot are separated by 20 pixels, or 2.4 μm. Top (a) in-plane density $n = 0.0569$ in the intermediate region; bottom (b) $n = 0.0563$ lower-density intermediate region just before the fluid. Compare the 2D situation with that in 3D in Fig. 3.

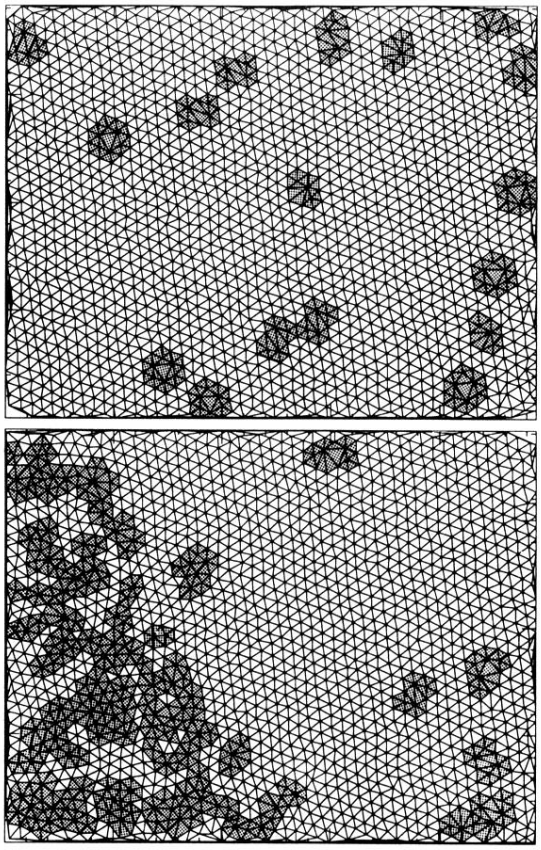

FIG. 2. Delaunay triangulations of snapshots containing instantaneous particle positions for the 3D run. The center of each particle in the image is at a vertex with nearest neighbor-bonds shown by the lines. Defects in the topology of the lattice, or particles that are not sixfold coordinated, are highlighted by having their near neighborhoods shaded. Tic marks on the borders of each snapshot are separated by 20 pixels, or 2.4 μm. Top (a) in-plane density $n = 0.0599$ just into crystal; bottom (b) $n = 0.0587$ just into intermediate region. Note the relatively sharp interface between order and disorder on the left-hand side of (b).

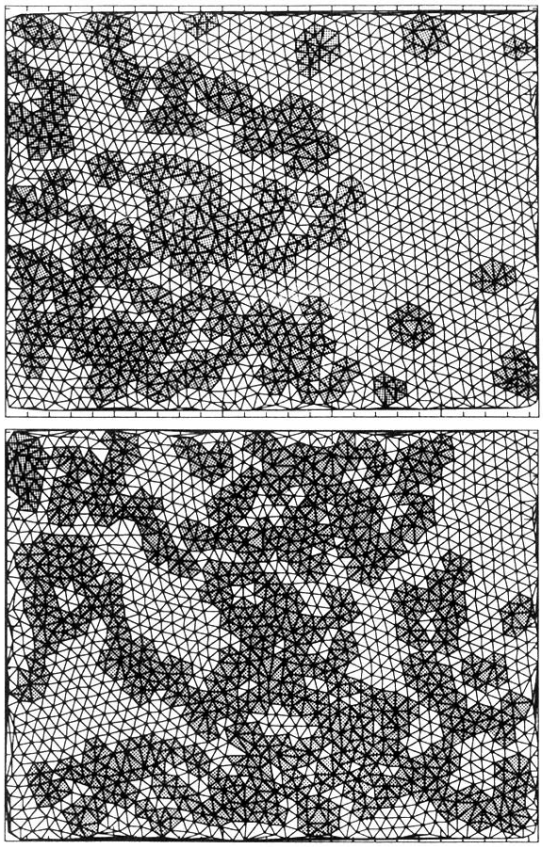

FIG. 3. Delaunay triangulations of snapshots containing instantaneous particle positions for the 3D run. The center of each particle in the image is at a vertex with nearest-neighbor bonds shown by the lines. Defects in the topology of the lattice, or particles that are not sixfold coordinated, are highlighted by having their near neighborhoods shaded. Tick marks on the borders of each snapshot are separated by 20 pixels, or 2.4 μm. Top (a) in-plane density $n = 0.0578$ in the intermediate region; bottom (b) $n = 0.0571$ lower-density intermediate region just before fluid. The sharp interface between order and disorder is still visible here.